ARTICLE

Check for updates

# Quantum simulation for topological Euler insulators

Wending Zhao[1,2], Yan-Bin Yang [1,2], Yue Jiang[1,2], Zhichao Mao [1], Weixuan Guo [1], Liyuan Qiu[1], Gangxi Wang[1], Lin Yao[1], Li He[1], Zichao Zhou [1✉], Yong Xu [1✉] & Luming Duan [1✉]

Although recent studies have established a powerful framework to search for and classify topological phases based on symmetry indicators, there exists a large class of fragile topology beyond the description. The Euler class characterizing the topology of two-dimensional real wave functions is an archetypal fragile topology underlying some important properties. However, as a minimum model of fragile topology, the two-dimensional topological Euler insulator consisting of three bands remains a significant challenge to be implemented in experiments. Here, we experimentally realize a three-band Hamiltonian to simulate a topological Euler insulator with a trapped-ion quantum simulator. Through quantum state tomography, we successfully evaluate the Euler class, Wilson loop flow, entanglement spectra and Berry phases to show the topological properties of the Hamiltonian. The flexibility of the trapped-ion quantum simulator further allows us to probe dynamical topological features including skyrmion-antiskyrmion pairs and Hopf links in momentum-time space from quench dynamics.

[1] Center for Quantum Information, Institute for Interdisciplinary Information Sciences, Tsinghua University, Beijing 100084, PR China. [2] These authors contributed equally: Wending Zhao, Yan-Bin Yang and Yue Jiang. ✉email: zichaozhou@mail.tsinghua.edu.cn; yongxuphy@mail.tsinghua.edu.cn; lmduan@tsinghua.edu.cn

Topological phases have seen a rapid progress over the past two decades[1–5]. In particular, the ten-fold classification based on the $K$-theory represents a cornerstone in the description of topological phases[6–8]. Besides the internal symmetries, crystalline symmetries greatly enrich the classification of topological phases[9–12]. Remarkably, recent efforts have led to the development of a powerful framework based on symmetry indicators to categorize topological crystalline insulators[13–15]. However, a large class of topological phases falls outside the description[16–22]. Such a phase belongs to the category of so-called fragile topology that can be trivialized by adding trivial bands[16], in stark contrast to a stable topology which remains nontrivial upon adding trivial bands. In this context, a class of topological phases protected by space-time inversion symmetry is highlighted[20,22–29]. Among them, the Euler class characterizing the topological property of two-dimensional real wave functions underlies the failure of the Nielsen-Ninomiya theorem[20] and the existence of Wilson loop winding[22]. Yet, adding a trivial band can annihilate crossing nodes through braiding and remove the Wilson loop winding, showing a fragile topology of the Euler class. Such a fragile topology is theoretically shown to protect the nonzero superfluid weight in twisted bilayer graphene[30]. Despite recent important progress on experimental characterizations of the fragile topology in an acoustic metamaterial[31], the implementation of the topological Euler insulator[32,33] as a minimum model of fragile topology poses a significant experimental challenge.

Quantum simulators have been proven to be powerful platforms for experimentally studying topological phases. During the past decade, there have been great advances in simulating various topological phases via different quantum simulators including cold atom systems[34–40], solid-state spin systems[41–45], and superconducting circuits[46–49]. Trapped ions provide an alternative flexible platform to perform quantum simulations due to its state-of-the-art technologies to control and measure[50,51], enabling us to use it to simulate exotic topological phases and directly probe their intriguing topological properties through measurements with high precision.

In the article, we experimentally implement a three-band topological Euler Hamiltonian in momentum space using a single $^{171}$Yb$^+$ ion trapped in an electrode-surface trap as shown in Fig. 1. By measuring the momentum-resolved eigenstates through quantum state tomography, we evaluate the Euler class $\xi$, Wilson loop flow, and entanglement spectra to identify the band topology. With the Euler class, there are $2\xi$ protected crossing nodes between the two lowest energy bands. Such nodes can be annihilated either by closing the gap between the second and third bands or by adding a trivial band, followed by intricate braiding of crossing nodes[20,26,29]. Our further measurements of the Berry phases along four distinct closed trajectories illustrate the existence of four crossing points. Apart from the equilibrium topological properties, it has been theoretically demonstrated that skyrmion-antiskyrmion pairs and Hopf links appear in momentum-time space from quench dynamics for the post-quench three-band topological Euler Hamiltonian[32]. We experimentally observe the skyrmion-antiskyrmion pairs and Hopf links by measuring the time-evolving states under the Euler Hamiltonian.

## Results

### Model Hamiltonian and experimental realization.
We start by considering the following three-band Hamiltonian for Euler insulators in momentum space, which will be experimentally engineered,

$$H(\mathbf{k}) = 2\mathbf{n}(\mathbf{k}) \cdot \mathbf{n}(\mathbf{k})^T - I, \tag{1}$$

where

$$
\begin{aligned}
\mathbf{n}(\mathbf{k}) &= \left( n_x(\mathbf{k}), n_y(\mathbf{k}), n_z(\mathbf{k}) \right)^T \\
&= \frac{1}{\mathcal{N}} \left( m - \cos(k_x) - \cos(k_y), \sin(k_x), \sin(k_y) \right)^T
\end{aligned}
\tag{2}
$$

is a real unit vector at $\mathbf{k} = (k_x, k_y)$ in the two-dimensional (2D) Brillouin zone. Here, $\mathcal{N}$ is the normalization factor, and $m$ is a parameter with $|m| \neq 0, 2$ for $H(\mathbf{k})$ to be well-defined. The Hamiltonian is a real symmetric matrix and thus respects $C_2\mathcal{T}$ (composition of twofold rotational and time-reversal operators) symmetry, which can be represented by the complex conjugation $\mathcal{K}$ in a suitable basis[26]. For simplicity, we have flattened the spectrum of the Hamiltonian without affecting the band topology. The Hamiltonian has two degenerate bands $|u_{1,2}(\mathbf{k})\rangle = \mathbf{u}_{1,2}(\mathbf{k})$ with eigenenergy $E_{1,2} = -1$ and one band $|u_3(\mathbf{k})\rangle = \mathbf{n}(\mathbf{k}) = \mathbf{u}_1(\mathbf{k}) \times \mathbf{u}_2(\mathbf{k})$ with eigenenergy $E_3 = 1$. The eigenstates are real unit vectors because of the reality of the Hamiltonian.

We implement the Euler Hamiltonian $H(\mathbf{k})$ in momentum space through microwave operations on three hyperfine states $|1\rangle = |F = 0, m_F = 0\rangle$, $|2\rangle = |F = 1, m_F = -1\rangle$, and $|3\rangle = |F = 1, m_F = 0\rangle$ in the $^2S_{1/2}$ manifold using a single $^{171}$Yb$^+$ ion trapped in an electrode-surface chip trap as shown in Fig. 1 (see Subsection "Experimental setup" in Methods for details). Specifically, we drive the transition between the $|1\rangle$ and $|2\rangle$ levels or the transition between the $|1\rangle$ and $|3\rangle$ levels by near resonant microwaves and drive the transition between the $|2\rangle$ and $|3\rangle$ levels by two far-detuned microwaves through microwave Raman transitions. In the experiment, we implement the Hamiltonian $H_{\text{exp}}(\mathbf{k})$ which has the same eigenstates as $H(\mathbf{k})$ and thus is topologically equivalent to $H(\mathbf{k})$ (see Subsection "Microwave operations in the trapped-ion system" in Methods for details). To measure the band topology of $H_{\text{exp}}(\mathbf{k})$, we first prepare the ion in the $|1\rangle$ state and then slowly vary the Hamiltonian to $H_{\text{exp}}(\mathbf{k})$. Since $|1\rangle$ is the highest energy eigenstate $|u_3(\mathbf{k}^*)\rangle$ of our initial Hamiltonian $H(\mathbf{k}^*)$ at high-symmetry points $\mathbf{k}^*$ in momentum space, the state can evolve to its highest energy eigenstate $|u_3(\mathbf{k})\rangle$ of $H_{\text{exp}}(\mathbf{k})$ at the momentum $\mathbf{k}$ over the adiabatic passage (see Subsection "Adiabatic passage" in Methods for details). At the end, we employ quantum state tomography to measure the density matrix $\rho(\mathbf{k})$ (see Subsection "Quantum state tomography for a qutrit system" in Methods for details) and take the real state closest to $\rho(\mathbf{k})$ as the measured state for $|u_3(\mathbf{k})\rangle$ (see Subsection "The real state from the measured density matrix" in Methods for details). For the adiabatic preparation, the average fidelities are $\overline{F} = 97.1\%$ and $\overline{F} = 96.9\%$ for the topologically nontrivial ($m = 1$) and trivial phases ($m = 3$), respectively (see Subsection "The fidelity of the measured state" in Methods for detailed discussion). Since $|u_3(\mathbf{k})\rangle$ contains full information of the flattened Hamiltonian $H(\mathbf{k})$, we can thus determine the topological properties of the Euler Hamiltonian using these measured states.

### Euler class.
The band topology of a Euler insulator can be characterized by the Euler class[20,23,24,26]

$$\xi = \frac{1}{2\pi} \int_{\text{BZ}} \mathrm{d}^2\mathbf{k} (\langle \partial_{k_x} u_1 | \partial_{k_y} u_2 \rangle - \langle \partial_{k_y} u_1 | \partial_{k_x} u_2 \rangle) \tag{3}$$

for the two occupied bands $|u_1\rangle$ and $|u_2\rangle$. It is enforced to be quantized by the reality of eigenstates due to $C_2\mathcal{T}$ symmetry. To well define the Euler class, we require that the two occupied bands form an orientable real vector bundle, which is ensured by the vanishing of Berry phases along any noncontractible loops for the
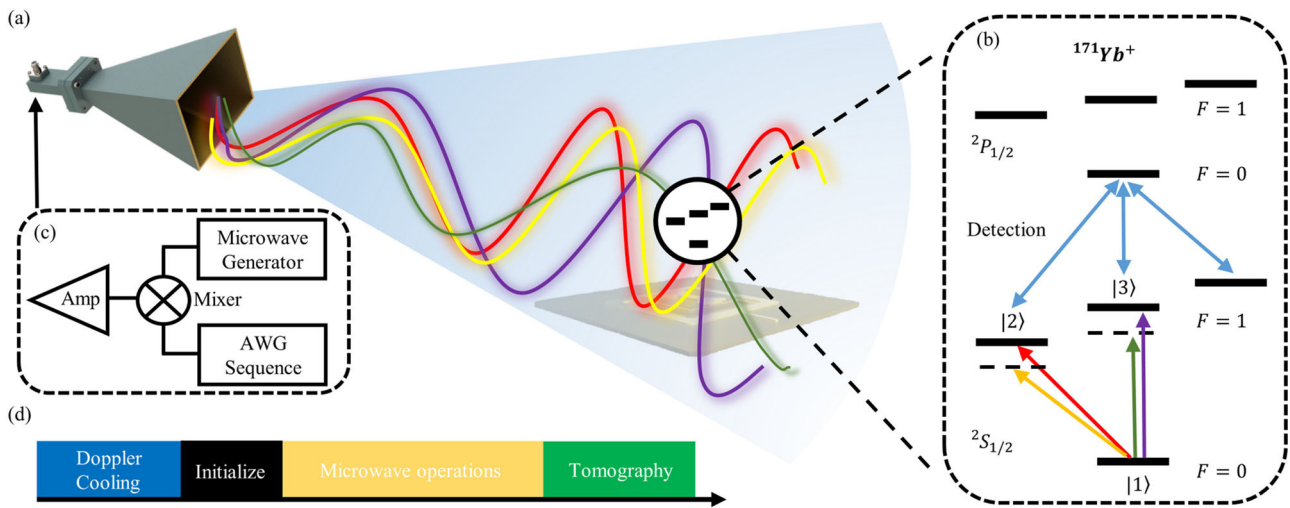
**Fig. 1 Experimental scheme for observing topological Euler insulators with a trapped ion. a** Schematic of our experimental setup. A single $^{171}$Yb$^+$ ion is trapped in a surface-electrode chip trap. **b** The energy level structure of the $^{171}$Yb$^+$ ion. The three states $|1\rangle$, $|2\rangle$, and $|3\rangle$ for the Hamiltonian are encoded in the hyperfine states $|F = 0, m_F = 0\rangle$, $|F = 1, m_F = -1\rangle$, and $|F = 1, m_F = 0\rangle$, respectively. Quantum operations and adiabatic evolutions are implemented by microwaves. Two far-detuned microwave pulses (denoted by yellow and green arrows) are used for Raman transitions between the levels $|2\rangle$ and $|3\rangle$. The quantum state projected to $|2\rangle$ or $|3\rangle$ generates fluorescence detected by a 370 nm detection beam. **c** Schematic of our microwave setup. The microwaves are generated by an arbitrary waveform generator (AWG) controlled by a computer according to the sequence mixed with a high-frequency microwave signal. They are shone on the ion through a microwave horn. **d** Experimental sequences. The ion is firstly cooled through the Doppler cooling for 2 ms and then initialized to the dark state by optical pumping, which typically takes $2-3\,\mu$s. We then follow the adiabatic passage to slowly tune the Hamiltonian by microwave operations so as to drive the state to an eigenstate of $H(\mathbf{k})$ at any momentum point in the 2D Brillouin zone. The adiabatic passage typically takes $200-300\,\mu$s, and at some momentum points it may take up to $500\,\mu$s (see Subsections "Microwave operations in the trapped-ion system" and "Adiabatic passage" in Methods for more details). At the end, we perform the quantum state tomography to obtain the full density matrix of the final state (see Subsection "Quantum state tomography for a qutrit system" in Methods for more details).

occupied space[20,22,26]. For a three-band Euler Hamiltonian, the Euler class can be reduced to another form[26]

$$\xi = \frac{1}{2\pi} \int_{\mathrm{BZ}} \mathrm{d}^2 \mathbf{k} [\mathbf{n} \cdot (\partial_{k_x} \mathbf{n} \times \partial_{k_y} \mathbf{n})], \qquad (4)$$

showing that $\xi$ is equal to twice of the winding number (Pontryagin number) of $\mathbf{n}(\mathbf{k})$ over the 2D Brillouin zone (see Supplementary Note 1). In other words, the Euler class is determined by twice of times that $\mathbf{n}(\mathbf{k})$ wraps the sphere $S^2$, which also implies that the Euler class for a three-band Hamiltonian should be an even integer. Note that if the orientations of all vectors $\mathbf{n}(\mathbf{k})$ are reversed, we obtain the same Hamiltonian but the opposite winding for $\mathbf{n}(\mathbf{k})$, showing that the sign of $\xi$ is ambiguous and only its absolute value characterizes the topology[22]. With the relation between the Euler class $\xi$ and the winding number of $\mathbf{n}(\mathbf{k})$, we can obtain the phase diagram that the Euler Hamiltonian $H(\mathbf{k})$ in Eq. (1) is topologically nontrivial with $\xi = 2$ for $0 < |m| < 2$ and trivial with $\xi = 0$ for $|m| > 2$.

Our experimentally measured vectors $\mathbf{n}(\mathbf{k})$ in a topological phase indeed exhibit a skyrmion structure over the Brillouin zone [see Fig. 2(a)] wrapping the entire sphere once [see Fig. 2(b)], which suggests that the Euler class $\xi = 2$ for the experimentally realized Hamiltonian. To be more quantitative, we map the measured vectors to a two-band Chern insulator by $H_C(\mathbf{k}) = \mathbf{n}(\mathbf{k}) \cdot \boldsymbol{\sigma}$ with Pauli matrices $\boldsymbol{\sigma} = (\sigma_x, \sigma_y, \sigma_z)$. The fact that the Euler class is equal to twice of the Chern number of $H_C(\mathbf{k})$ allows us to determine the Euler class by computing the Chern number, which is much more efficient than directly performing the integral for Eq. (4) (see more details in Supplementary Note 1). We find that the Chern number calculated using the measured $\mathbf{n}(\mathbf{k})$ is equal to 1 so that $\xi = 2$. In comparison, we also display the measured vectors $\mathbf{n}(\mathbf{k})$ in a trivial phase, which do not form a skyrmion
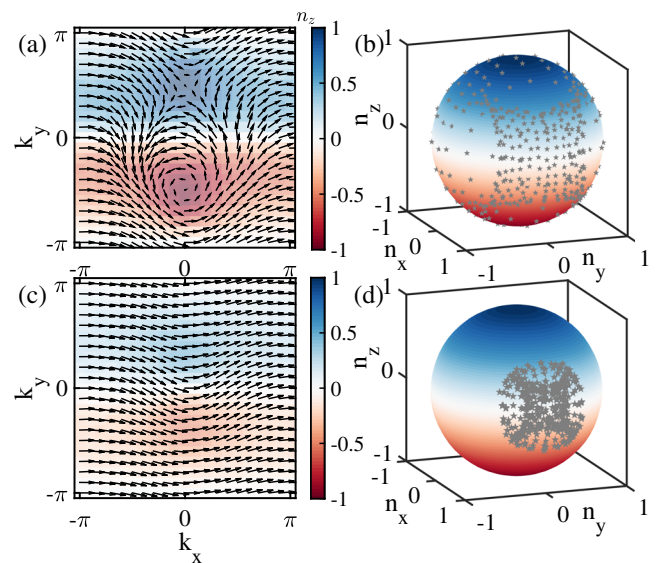


**Fig. 2 Measurements of the Euler class. a** The experimentally measured vectors $\mathbf{n}(\mathbf{k})$ for the Euler Hamiltonian $H(\mathbf{k})$ in Eq. (1) with $m = 1$ (corresponding to a nontrivial Hamiltonian) over a $20 \times 20$ discretized Brillouin zone and **b** their distribution on the sphere $S^2$. **c** The experimentally measured vectors $\mathbf{n}(\mathbf{k})$ for the Euler Hamiltonian $H(\mathbf{k})$ in Eq. (1) with $m = 3$ (corresponding to a trivial Hamiltonian) over a $20 \times 20$ discretized Brillouin zone and **d** their distribution on the sphere $S^2$. In the nontrivial case, the vectors $\mathbf{n}(\mathbf{k})$ exhibit a nontrivial skyrmion structure and cover the entire sphere once, yielding a nonzero Euler class $\xi = 2$, whereas in the trivial case, the vectors cover parts of the sphere, yielding a zero Euler class.

structure [see Fig. 2(c)] and cover only parts of the sphere [see Fig. 2(d)], indicating that $\xi = 0$.

**Wilson loops and entanglement spectra.** The Wilson loop provides a powerful framework to characterize the fragile topology[17,19,20,22]. However, it is very challenging to make an experimental measurement of it. In the trapped-ion quantum simulator, the quantum state tomography technique allows us to evaluate the Wilson loop based on the measured eigenstates of a Euler Hamiltonian.

Specifically, the $x$-directed Wilson loop $\mathcal{W}_x$ with the base point $\boldsymbol{k}_0 = (k_x, k_y)$ can be computed in a $N \times N$ discretized Brillouin zone as[52,53]

$$[\mathcal{W}_x]_{mn} = \langle u_m(\boldsymbol{k}_0) | \prod_{\boldsymbol{k}_j}^{\boldsymbol{k}_N \leftarrow \boldsymbol{k}_1} P_{\mathrm{occ}}(\boldsymbol{k}_j) | u_n(\boldsymbol{k}_0) \rangle, \quad (5)$$

where $\boldsymbol{k}_j = (k_x + \frac{2\pi j}{N}, k_y)$, $N$ is the number of discrete momenta on the loop, and $P_{\mathrm{occ}}(\boldsymbol{k}_j)$ is the projector on the occupied bands at the momentum $\boldsymbol{k}_j$. The Wilson loop operator $\mathcal{W}_x$ is unitary so that its eigenvalues take the form of $e^{i\theta_x(k_y)}$ which only depends on $k_y$; $\theta_x(k_y)$ as a function of $k_y$ is known as the Wilson loop spectrum for $\mathcal{W}_x$. The $y$-directed Wilson loop $\mathcal{W}_y$ and the corresponding spectrum $\theta_y(k_x)$ can be defined similarly. For our three-band model, we only need the experimentally measured highest energy eigenstates to construct the occupied projectors in the Wilson loop,

$$P_{\mathrm{occ}}(\boldsymbol{k}_j) = I - |u_3(\boldsymbol{k}_j)\rangle\langle u_3(\boldsymbol{k}_j)|. \quad (6)$$

The Wilson loop spectrum can be determined by diagonalizing the matrix

$$P = \prod_{\boldsymbol{k}_j}^{\boldsymbol{k}_N \leftarrow \boldsymbol{k}_0} P_{\mathrm{occ}}(\boldsymbol{k}_j), \quad (7)$$

which gives us three eigenvalues as $\{e^{i\theta_x^{(1)}}, e^{i\theta_x^{(2)}}, 0\}$. Discarding the zero eigenvalue contributed by the unoccupied subspace, we obtain the Wilson loop eigenvalues $\{\theta_x^{(1)}, \theta_x^{(2)}\}$ for the two occupied bands.

For the Euler Hamiltonian with two occupied bands, due to the reality of eigenstates, the Wilson loop operator takes the form of $e^{i\theta\sigma_y}$, which has a pair of eigenvalues $e^{\pm i\theta}$. For a topological Euler insulator, both $\theta_x(k_y)$ and $\theta_y(k_x)$ exhibit a nontrivial winding, indicating an obstruction to the Wannier representation. The winding number is equivalent to the Euler class $\xi$[22].

Figure 3(a, b) shows the experimentally measured Wilson loop spectra $\theta_x(k_y)$ [$\theta_y(k_x)$ has similar behaviors], which are evaluated based on the measured highest energy eigenstates. In the topological phase, each branch of the Wilson loop spectra exhibits a winding number ($\pm 2$), whereas in the trivial phase, the winding patterns are not observed. All the experimental results are in excellent agreement with the theoretical ones. We remark that such a winding can be removed by adding a trivial band, which reveals the fragile topology feature of the system (see Supplementary Note 2 for more details).

Although we experimentally realize the topological Euler Hamiltonian in momentum space, we can extract the edge state information through the single-particle entanglement spectra evaluated based on the measured states; such spectra can exhibit more robust nontrivial features than those for physical boundaries in a topological band insulator[10,54,55].

Figure 3c displays the entanglement spectra $\mathrm{ES}_x(k_y)$ obtained by partially tracing out the right part of the system using the experimentally measured unoccupied eigenstates $|u_3(\boldsymbol{k})\rangle$ for the
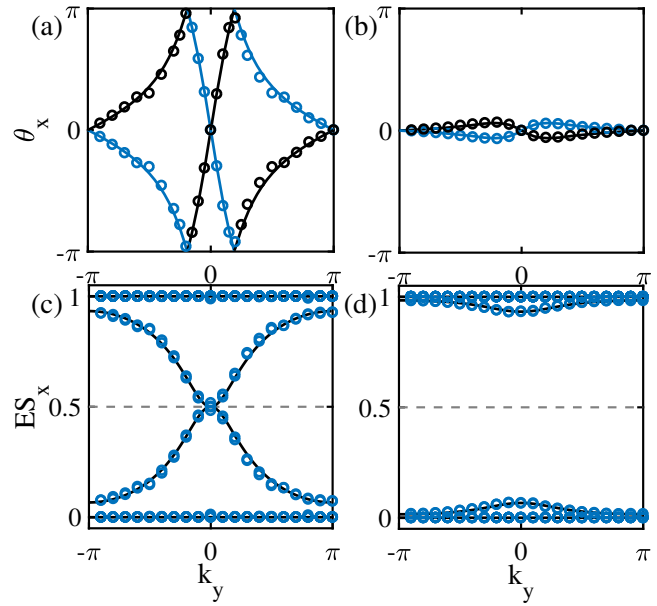


**Fig. 3 Observation of Wilson loop spectra and entanglement spectra. a**, **b** The experimentally measured Wilson loop spectra (solid circles) in comparison with the numerically calculated ones (solid lines). **c**, **d** The experimentally measured entanglement spectra (circles) in comparison with the numerical ones (solid lines). We consider the nontrivial Euler Hamiltonian $H(\boldsymbol{k})$ in Eq. (1) with $m = 1$ in **a**, **c** and the trivial one with $m = 3$ in **b**, **d**.

Euler Hamiltonian $H(\boldsymbol{k})$ (see Supplementary Note 3 for more details). In the topological phase, an in-gap spectrum with mid-gap modes near $\xi_n = 0.5$ arises in the entanglement spectra, which agrees very well with the theoretical prediction. The experimental results also support the theoretical prediction of the parabolic dispersion for the entanglement spectra near the mid-gap modes. In the trivial phase, our experimental results do not reveal the existence of gapless entanglement spectra, indicating that the phase is adiabatically connected to a trivial phase with zero entanglement entropy.

**Dirac points.** The Euler class $\xi$ is also manifested in the existence of $2\xi$ stable Dirac points between the two occupied bands[20,26]. They are protected by the $C_2\mathcal{T}$ symmetry and cannot be annihilated without the gap closing with the third band. To see this feature, we consider the following model by adding an extra term to $H(\boldsymbol{k})$ in Eq. (1) with $m = 1$,

$$H'(\boldsymbol{k}) = H(\boldsymbol{k}) + \mathrm{diag}(h_0(\boldsymbol{k}), h_+(\boldsymbol{k}), h_-(\boldsymbol{k})) \quad (8)$$

with $h_0(\boldsymbol{k}) = 0.1[\cos(k_y) - \cos(k_x)]$ and $h_\pm(\boldsymbol{k}) = h_0(\boldsymbol{k}) \pm 0.5$. The additional term lifts the degeneracy of the two occupied bands for the flattened Hamiltonian $H(\boldsymbol{k})$ except at the Dirac points as shown in Fig. 4(a). Due to the $C_2\mathcal{T}$ symmetry, a Dirac point between the two lowest bands yields a quantized Berry phase $\gamma = \pi$ for the lowest eigenstates $|u_1(\boldsymbol{k})\rangle$ along a closed path $l$ enclosing it.

Since the energy gap between the two lowest eigenstates on a path enclosing the Dirac point is opened, we can still use the adiabatic passage to realize the eigenstate $|u_1(\boldsymbol{k})\rangle$ at the momenta on the closed path. After that, we measure the states by quantum state tomography and then evaluate the Berry phase based on the measured states. We find that the experimentally evaluated Berry phase $\gamma = \pi$ on the four closed paths [see Fig. 4(b)], indicating the presence of a Dirac point inside each closed path.
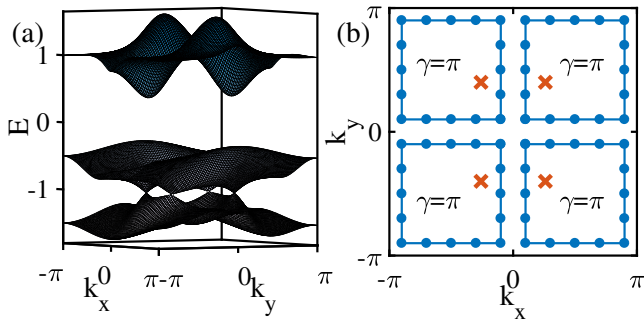
**Fig. 4 Measurements of the Berry phase. a** The theoretical energy spectrum of the Hamiltonian $H'(\mathbf{k})$ in Eq. (8) over the Brillouin zone, showing the existence of four Dirac points between the two lowest energy bands located at $\mathbf{k} = (k_x, k_y) \approx (\pm 0.26\pi, \pm 0.4\pi)$. (b) The experimentally measured Berry phases for the lowest energy eigenstate $|u_1(\mathbf{k})\rangle$ along four closed paths composed of discrete momenta (blue lines and points) in the Brillouin zone enclosing the corresponding Dirac points (red crosses). For each Dirac point, the measured Berry phase is $\gamma = \pi$.

**Quench dynamics**. Besides the equilibrium features, it has been theoretically shown that nonequilibrium dynamics provides another tool to uncover the static band topology of an Euler insulator[32]. Let us start from an initial state $\psi(\mathbf{k}, t = 0) = \psi_0 = (0, 0, 1)^T$ for each momentum $\mathbf{k}$, which can be seen as the eigenstate of a topologically trivial Euler Hamiltonian $H_0(\mathbf{k}) = \mathrm{diag}(-1, -1, 1)$. We consider the quench dynamics for the trivial initial state evolving under a postquench Euler Hamiltonian $H(\mathbf{k})$ in Eq. (1). Due to the flatness of $H(\mathbf{k})$ in Eq. (1), the state evolves as

$$\psi(\mathbf{k}, t) = [\cos(t) - i\sin(t)H(\mathbf{k})]\psi_0, \qquad (9)$$

which is periodic about time $t$ with a period $T = \pi$. The periodicity of the evolving state both in time $t$ and momentum $\mathbf{k}$ in 2D Brillouin zone makes the space of $(k_x, k_y, t)$ form a 3-torus $T^3$. In analogy to the quench dynamics of a two-band Chern insulator[56], one can construct a map $f$ from the $(k_x, k_y, t)$ space as a $T^3$ to a 2-sphere $S^2$ as follows. For a point $(k_x, k_y, t)$ on $T^3$, the image of the map $f(k_x, k_y, t)$ is a unit vector $\hat{\mathbf{p}} = (p_x, p_y, p_z)$ on $S^2$ as $\hat{\mathbf{p}} = \psi^\dagger(k_x, k_y, t)\boldsymbol{\mu}\psi(k_x, k_y, t)$, where $\boldsymbol{\mu} = (\mu_x, \mu_y, \mu_z)$ with $\mu_\nu$ ($\nu = x, y, z$) being a $3 \times 3$ matrix[32] (see Supplementary Note 4). Because the map $f$ from any $T^2$ cross-section of $(k_x, k_y, t)$ space to $S^2$ is trivial with zero Chern number, the map $f$ is equivalent to the form of a Hopf map from $S^3$ to $S^2$ classified by an integer called Hopf invariant[57,58]. In the quench dynamics of a topological Euler Hamiltonian, the Hopf invariant determines the linking number of a linking structure for the inverse images of the Hopf map[32].

The nontrivial linking structure for the quench dynamics of an Euler insulator is directly related to the static band topology of the postquench Hamiltonian[32]. To see this relation, we write the evolving state as

$$\psi(\mathbf{k}, t) = \cos(t)\psi_0 - i\sin(t)\mathbf{a}(\mathbf{k}). \qquad (10)$$

Here $\mathbf{a}(\mathbf{k}) = H(\mathbf{k})\psi_0 = i\psi(\mathbf{k}, t = \pi/2)$, which defines a map from the 2D Brillouin zone to $S^2$. Based on the static Hamiltonian $H(\mathbf{k})$ in Eq. (1), we obtain $\mathbf{a}(\mathbf{k}) = (2n_x(\mathbf{k})n_z(\mathbf{k}), 2n_y(\mathbf{k})n_z(\mathbf{k}), 2n_z^2(\mathbf{k}) - 1)^T$. By parameterizing $\mathbf{n}(\mathbf{k})$ with spherical coordinates as $\mathbf{n}(\mathbf{k}) = (\sin\alpha\cos\beta, \sin\alpha\cos\beta, \cos\alpha)$, we have $\mathbf{a}(\mathbf{k}) = (\sin 2\alpha\cos\beta, \sin 2\alpha\cos\beta, \cos 2\alpha)$. For a nontrivial Euler Hamiltonian with $\xi = 2$, $\mathbf{n}(\mathbf{k})$ fully cover the $S^2$ so that there exist 1D curves with $n_z(\mathbf{k}) = \cos\alpha(\mathbf{k}) = 0$ in the Brillouin zone on which $\mathbf{a}(\mathbf{k}) = (0, 0, -1)$; the curves divide the entire Brillouin zone into two patches.
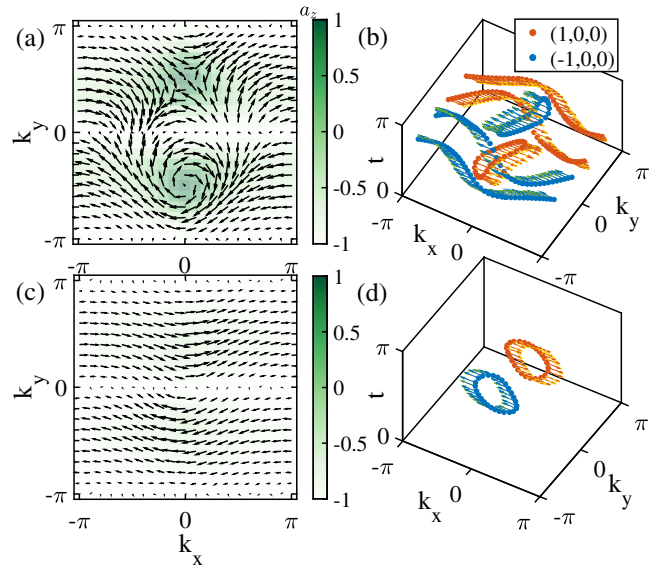


**Fig. 5 Measurements of dynamical topological structures from quench dynamics. a** The skyrmion-antiskyrmion structures for the vectors $\mathbf{a}(\mathbf{k})$ obtained by measuring the time-evolving state at $t = \pi/2$ under the nontrivial postquench Hamiltonian $H(\mathbf{k})$ with $m = 1$. The skyrmion or antiskyrmion structures appear in each half of the 2D Brillouin zone, contributing a Chern number of $\pm 1$, respectively. **b** The skyrmion and antiskyrmion structure is directly associated with the nontrivial linking structure with a link and an antilink composed of the inverse images $f^{-1}(\hat{\mathbf{p}}_1)$ and $f^{-1}(\hat{\mathbf{p}}_2)$ in $(k_x, k_y, t)$ space for any two distinct points $\hat{\mathbf{p}}_1$ and $\hat{\mathbf{p}}_2$ on $S^2$. Here we take $\hat{\mathbf{p}}_1 = (1, 0, 0)$ and $\hat{\mathbf{p}}_2 = (-1, 0, 0)$. The red and blue arrows show the images of the experimentally measured evolving state through the Hopf map, which are close to the theoretical values marked by yellow and green arrows. **c, d** Quench dynamics for the trivial postquench Hamiltonian $H(\mathbf{k})$ with $m = 3$. The vectors $\mathbf{a}(\mathbf{k})$ have a topologically trivial distribution and the inverse images of $\hat{\mathbf{p}}_1$ and $\hat{\mathbf{p}}_2$ do not link with each other. In **a** and **c**, the color bar describes $a_z$, the component of the vectors $\mathbf{a}(\mathbf{k})$ along the $z$ direction.

The curves also serve as fixed points for the dynamics where the initial state only picks up a global phase during the time evolution. By shrinking the curve into a single point, each of the two patches can be seen as a sphere. In this case, $\mathbf{a}(\mathbf{k})$ defines a map from $S^2$ to $S^2$ characterized by the winding number for each of these patches. Though the winding number of $\mathbf{a}(\mathbf{k})$ over the entire Brillouin zone is zero since the state $\psi(\mathbf{k}, t = \pi/2)$ is trivial, $\mathbf{a}(\mathbf{k})$ can wrap the sphere $S^2$ once in each patch[32]. The nontrivial winding of $\mathbf{a}(\mathbf{k})$ over each patch is associated with the Hopf link in the quench dynamics of the patch, similar to the correspondence between the static Chern number and the existence of the dynamical Hopf link for quench dynamics of a Chern insulator (see Supplementary Note 4).

Figure 5 shows our experimentally measured vectors $\mathbf{a}(\mathbf{k})$ and linking structures. Specifically, we first prepare the ion in the $|3\rangle$ level and then measure the density matrix $\rho(\mathbf{k}, t)$ of the time-evolving state for a momentum in the Brillouin zone via quantum state tomography after the unitary time evolution under the experimentally engineered Euler Hamiltonian. We then evaluate $\mathbf{a}(\mathbf{k})$ and the images of the Hopf map, that is, $\langle \mu_i \rangle = \mathrm{Tr}(\rho(\mathbf{k}, t)\mu_i)$ with $i = x, y, z$ based on the measured density matrices. For the nontrivial postquench Euler Hamiltonian, the experimentally measured $\mathbf{a}(\mathbf{k})$ exhibit a nontrivial skyrmion and antiskyrmion structure in the upper and lower halves of the Brillouin zone divided by the curves $k_y = 0, \pi$ with $n_z(\mathbf{k}) = 0$, as shown in Fig. 5(a). To quantitatively identify the skyrmion and antiskyrmion structure of the measured $\mathbf{a}(\mathbf{k})$, we construct a model $H_C(\mathbf{k}) = \mathbf{a}(\mathbf{k}) \cdot \boldsymbol{\sigma}$ for each of the two patches and find that the

Chern numbers are equal to ±1, which are in excellent agreement with the theoretical results. The pair of skyrmions in the Brillouin zone leads to a pair of links with opposite signs for the inverse images in the corresponding regions of the $(k_x, k_y, t)$ space (see Supplementary Note 4), which are experimentally demonstrated in Fig. 5(b). This also indicates the nontrivial band topology of the postquench Hamiltonian. For a trivial postquench Hamiltonian, the measured $a(k)$ do not fully cover $S^2$ for the two patches of the Brillouin zone, and the inverse image have no linking structures, as shown in Fig. 5(c) and (d).

## Conclusions

We have experimentally realized a minimum Bloch Hamiltonian for topological Euler insulators protected by $C_2\mathcal{T}$ symmetry in a trapped-ion qutrit system and identified its band topology by evaluating the Euler class, Wilson loop flow, entanglement spectra and the Berry phases based on the measured states via quantum state tomography. We further observed the nontrivial dynamical topological structures including the skyrmion-antiskyrmion structures and Hopf links during the unitary evolution under the topological Euler Hamiltonian. Our work opens the door for further studying fragile topological phases using quantum simulation technologies.

## Methods

**Experimental setup**. We use 399 nm and 370 nm laser beams to ionize the ytterbium (Yb) atom and use a linear radio-frequency Paul trap driven at 20.27 MHz (realized by a surface-electrode chip) to trap a single $^{171}Yb^+$ ion. The surface trap is designed and fabricated in our group at CQI, IIIS, Tsinghua University by following previous works[59–61]. In our case, we make some modifications to dimensions of electrodes and the number of segmented electrodes in order to achieve a higher ability in controlling ion's motion (see detailed presentation in Section A of Supplementary Note 5). The Doppler cooling, the optical pumping and the detection are implemented by 370 nm laser beams, which are modulated by acousto-optic modulators and electro-optic modulators. We also shine a 935 nm laser beam to repump the ion from the $^2D_{3/2}$ manifold back to the $^2S_{1/2}$ manifold in case that the ion decays to the $^2D_{3/2}$ manifold through spontaneous emission. After the ion is prepared in the dark state via optical pumping, we slowly vary the Hamiltonian through microwave operations. In the experiment, a magnetic field is applied to the system to split the $|2\rangle$ and $|3\rangle$ levels so that we can individually control the couplings between the hyperfine states through microwave operations. To control the amplitude and phase of microwaves, we use an arbitrary waveform generator mixed with a high-frequency signal to modulate them. In order to implement an arbitrary experimental sequence, a field programmable gate array is employed to control acousto-optic modulators, electro-optic modulators, arbitrary waveform generators and a photo-multiplier tube. At the end, we perform measurements by collecting the state-dependent fluorescence emission by an objective with a 0.33 numerical aperture and a photo-multiplier tube; the detection fidelities for the dark state and the bright state are 99.4% and 98.1%, respectively (see Section C of Supplementary Note 5 for detailed discussions on how the detection fidelities and their statistical uncertainties are estimated). For more detailed discussion on laser and microwave setups and detection, see Section B and C of Supplementary Note 5.

**Microwave operations in the trapped-ion system**. In our trapped-ion system, we simultaneously shine microwave radiations with four different frequencies on the trapped ion to implement the three-band Hamiltonian. The microwave pulses are generated by a high-frequency generator and modulated by an arbitrary waveform generator mixed by an in-phase and quadrature mixer. In the presence of a magnetic field and the microwaves, the trapped-ion qutrit system is described by the Hamiltonian

$$\hat{H} = \hat{H}_0 + \hat{H}_{AL}, \tag{11}$$

where the atomic part is

$$\hat{H}_0 = \hbar(\omega_{hf} - \omega_z)|2\rangle\langle 2| + \hbar(\omega_{hf} + \omega_q)|3\rangle\langle 3| \tag{12}$$

with $\omega_{hf}$ being the central transition frequency between $|1\rangle$ and $|3\rangle$, and $\omega_z$ ($\omega_q$) being the frequency of the first-order (second-order) Zeeman energy determined by magnetic fields. The interaction part due to the microwaves is

$$\hat{H}_{AL}(t) = \sum_{n=1}^{4} \sum_{j=2,3} \hbar\Omega_{1j}^{(n)} \cos(\omega_n t + \phi_n)\hat{\sigma}_x^{(j)}, \tag{13}$$

where $\hat{\sigma}_x^{(j)} = |1\rangle\langle j| + H.c.$, $\omega_n$ and $\phi_n$ are the frequency and initial phase of each microwave, and $\Omega_{ij}^{(n)}$ is the Rabi frequency for the $|i\rangle \leftrightarrow |j\rangle$ transition driven by the $n$th microwave. We then derive the effective Hamiltonian $H_{exp}$ (see Eq. S41 in Supplementary Note 6) by following the method introduced in ref.[62] (see the

detailed derivation in Supplementary Note 6). To ensure that the Rabi rate is always a linear function of the power of a radio-frequency signal, we set the maximum Rabi rates in our experiments as $\Omega_{12} = (2\pi) \times 55.6$ kHz and $\Omega_{13} = (2\pi) \times 50.2$ kHz. The errors of $\Omega_{12}$ and $\Omega_{13}$ are 0.036 kHz and 0.038 kHz, respectively, obtained by fitting the Rabi oscillations with time (the time step is 0.5 μs and the number of repetitions at each data point is 5000). To simulate the Hamiltonian $H(k)$ at each $k$, in the experiment, we in fact implement the Hamiltonian

$$H_{exp}(k) = c(k)[H(k) - bI_3] \tag{14}$$

where $I_3$ is the $3 \times 3$ identity matrix. Clearly, this Hamiltonian has the same eigenstates as $H(k)$ and thus is topologically equivalent to $H(k)$. Here, $c(k)$ is a real positive parameter that needs to be numerically determined, and it may be different at different $k$. Given the fact that the required evolution time for the adiabatic passage in the experiment is proportional to $1/c(k)$ and our coherent time is finite, for a fixed $H(k)$, we find the minimum of $1/c(k)$ [or the maximum of $c(k)$] by solving Eq. (14) via the fmincon function in MATLAB. Since $H_{exp}(k)$ is a function of the Rabi frequencies, the detuning and the phases of microwaves, by solving Eq. (14), we obtain their values. In solving the equation, we also add some constraints on the microwave parameters. The far detuning for the Raman transition is set in the range from $(2\pi) \times 175.7$ kHz to $(2\pi) \times 326.3$ kHz, and the near detuning is set below $(2\pi) \times 10.0$ kHz in most cases. In light of the fact that the Rabi frequency of the Raman transition is only about 1/10 of the direct resonant Rabi flopping, we usually need much higher power for the far detuning microwaves than that of the near detuning microwaves. Based on this fact, we set the power of the two far detuning microwaves below $W_{1(2)}$, where $W_{1(2)}$ corresponds to the maximal power of a resonant microwave used to generate the maximal Rabi rate $\Omega_{12(13)}$. Meanwhile, we set the two near detuning microwaves below $0.2W_{1(2)}$ in most cases. With these constraints, we obtain a set of microwave parameters, and based on these parameters we realize the Hamiltonian $H_{exp}(k)$ in experiments.

In addition, the maximum value of the coupling between $|2\rangle$ and $|3\rangle$ that we can reach in the experiment is much smaller than the values of the couplings between $|1\rangle$ and $|2\rangle$ or $|1\rangle$ and $|3\rangle$, since the former coupling is realized through microwave Raman transitions. When $H_{23}$ is much larger than $H_{12}$ or $H_{13}$ in $H(k)$, the energy scale $c$ is very small so that a much longer period of time is required for the adiabatic evolution. To overcome the difficulty, we apply a $\pi$-rotation between $|1\rangle$ and $|2\rangle$ (or $|1\rangle$ and $|3\rangle$) at an appropriate moment during the adiabatic passage to change the basis for the qutrit system. The resultant effective Hamiltonian relative to the new basis has a smaller entry $H_{23}$ so that a larger value of the coefficient $c$ is obtained, which effectively reduces the time for the adiabatic evolution. Meanwhile, we continue the adiabatic passage for the Hamiltonian relative to the new basis and apply another $\pi$-rotation in detections for quantum state tomography.

**Adiabatic passage**. To measure the topological properties of the engineered Euler Hamiltonian, we first prepare the ion in the dark state $|1\rangle$, which is the highest energy eigenstate of the Hamiltonian $H(k)$ at high-symmetry points in momentum space,

$$k^* = (k_x, k_y) \in \{(0,0), (0,\pi), (\pi,0), (\pi,\pi)\}. \tag{15}$$

To prepare the ion in the highest energy eigenstate of $H(k)$, we choose a starting point $k^*$ in the set of high-symmetry points so that the path in the Brillouin zone from $k^*$ to the final point $k$ is the shortest. We then slowly vary the Hamiltonian to the final one $H_{exp}(k)$ through the shortest path. Specifically, we divide the path into $N = |k - k^*|/\Delta k$ parts ($\Delta k = \pi\sqrt{2}/400$), and at each part $k_n = [(k - k^*)/|k - k^*|] n\Delta k + k^*$ with $n = 1, 2, \cdots, N$, the associated Hamiltonian is $H_{exp}(k_n)$, where $c(k_n)$ is numerically calculated by solving Eq. (14). We then vary the microwave parameters so that at time $t_n = \sum_{j=1}^{n-1} T_j$ [$T_j$ indicates the duration over which the Hamiltonian stays at $H_{exp}(k_{j+1})$], the implemented Hamiltonian is $H_{exp}(k_n)$. To optimize the adiabatic evolution, we set $T_n = \alpha_n/c(k_n)$ where $\alpha_n$ may vary from 10 to 50. Each segment typically takes 1–2 μs. The total process typically takes 200–300 μs, and at some momentum points it may take up to 500 μs. After the adiabatic passage, we obtain a state which is very close to the highest eigenstate of $H_{exp}(k)$. We then measure the final states by quantum state tomography, based on which the topological properties are identified.

**Quantum state tomography for a qutrit system**. At the end of microwave operations, we perform a quantum state tomography to obtain the full density matrix of the qutrit system[42,63]. The density matrix can be written in terms of eight unknown real variables as

$$\rho = \begin{pmatrix} a & c+id & g+ih \\ c-id & b & e+if \\ g-ih & e-if & 1-a-b \end{pmatrix}. \tag{16}$$

Since the probability $P_1$ in the dark state relative to eight different bases realized by applying $\pi$ or $\pi/2$ or both rotations on Bloch spheres is a linear function of these variables (see Table I in Supplementary Note 7), we can determine them by solving the linear equations after we obtain the probabilities. In experiments, each probability is measured by counting the number of occurrences of the dark state

over 4400 repeated experiments; the dark state is experimentally identified through the threshold method (see Section C of Supplementary Note 5 and the references therein for the introduction of the threshold method). We also employ the maximum likelihood estimation to find the best estimate for the physical density matrix. For the quantum state tomography and the maximum likelihood estimation, see Supplementary Note 7 for more details.

**The fidelity of the measured state**. We calculate the fidelity for the measured density matrix by

$$F(\boldsymbol{k}) = \langle \psi(\boldsymbol{k}) | \rho(\boldsymbol{k}) | \psi(\boldsymbol{k}) \rangle, \qquad (17)$$

where $\psi(\boldsymbol{k})$ is the theoretically obtained state, and $\rho(\boldsymbol{k})$ is the measured density matrix optimized by the maximum likelihood estimation. With the optimization, the average fidelities over $20 \times 20$ momentum points are $\overline{F} = 97.1\%$ and $\overline{F} = 96.9\%$ for the topologically nontrivial ($m = 1$) and trivial phases ($m = 3$), respectively (see the details on how to determine the average fidelity in Supplementary Note 7).

The infidelity may arise from the detection infidelity of the dark state or the bright state, microwave pulse errors caused by nonlinear effects of experimental equipments and environment fluctuations. In addition, de-coherence is also a factor for infidelity when the microwave operations take a long period of time. Note that de-coherence usually does not occur significantly within $600\,\mu s$ in our trapped-ion system, which is mainly restricted by the Zeeman state. In the experiment, we perform calibrations and optimize the experiment setups per hour in order to obtain a high fidelity.

**The real state from the measured density matrix**. To identify the band topology of the Euler Hamiltonian, we need to transform the measured density matrix $\rho$ into a real state $|\psi\rangle = (\alpha, \beta, \gamma)^T$ by maximizing the function

$$f(\alpha, \beta, \gamma) = |\langle \psi | \rho | \psi \rangle| \qquad (18)$$

so that $|\psi\rangle$ is the closest real state to the measured density matrix $\rho$. We find that the average fidelities between the real state $|\psi\rangle$ and the density matrix $\rho$ are 97.4% and 97.1% when $m = 1$ (nontrivial) and $m = 3$ (trivial), respectively. We also find that the fidelities between the closest complex pure states and the density matrix are 97.5% and 97.3%, respectively. We see that the infidelity resulted from the restriction to a real state rather than a general complex pure state in the above maximization is below 1%, suggesting that the measured density matrix may not correspond to a pure state due to decoherence and detection errors.

## Data availability

The data that support the findings of this study are available from the authors upon request.

## References

1. Hasan, M. Z. & Kane, C. L. Colloquium: topological insulators. *Rev. Mod. Phys.* **82**, 3045 (2010).
2. Qi, X.-L. & Zhang, S.-C. Topological insulators and superconductors. *Rev. Mod. Phys.* **83**, 1057 (2011).
3. Chiu, C.-K., Teo, J. C. Y., Schnyder, A. P. & Ryu, S. Classification of topological quantum matter with symmetries. *Rev. Mod. Phys.* **88**, 035005 (2016).
4. Wen, X.-G. Colloquium: Zoo of quantum-topological phases of matter. *Rev. Mod. Phys.* **89**, 041004 (2017).
5. Armitage, N. P., Mele, E. J. & Vishwanath, A. Weyl and Dirac semimetals in three-dimensional solids. *Rev. Mod. Phys.* **90**, 015001 (2018).
6. Schnyder, A. P., Ryu, S., Furusaki, A. & Ludwig, A. W. W. Classification of topological insulators and superconductors in three spatial dimensions. *Phys. Rev. B* **78**, 195125 (2008).
7. Kitaev, A. Periodic table for topological insulators and superconductors. *AIP Conf. Proc.* **1134**, 22–30 (2009).
8. Ryu, S., Schnyder, A. P., Furusaki, A. & Ludwig, A. W. W. Topological insulators and superconductors: tenfold way and dimensional hierarchy. *N. J. Phys.* **12**, 065010 (2010).
9. Fu, L. Topological crystalline insulators. *Phys. Rev. Lett.* **106**, 106802 (2011).
10. Hughes, T. L., Prodan, E. & Bernevig, B. A. Inversion-symmetric topological insulators. *Phys. Rev. B* **83**, 245132 (2011).
11. Slager, R.-J., Mesaros, A., Juričić, V. & Zaanen, J. The space group classification of topological band-insulators. *Nat. Phys.* **9**, 98–102 (2013).
12. Shiozaki, K. & Sato, M. Topology of crystalline insulators and superconductors. *Phys. Rev. B* **90**, 165114 (2014).
13. Po, H. C., Vishwanath, A. & Watanabe, H. Symmetry-based indicators of band topology in the 230 space groups. *Nat. Commun.* **8**, 50 (2017).
14. Bradlyn, B. et al. Topological quantum chemistry. *Nature* **547**, 298–305 (2017).
15. Kruthoff, J., de Boer, J., van Wezel, J., Kane, C. L. & Slager, R.-J. Topological classification of crystalline insulators through band structure combinatorics. *Phys. Rev. X* **7**, 041069 (2017).
16. Po, H. C., Watanabe, H. & Vishwanath, A. Fragile topology and wannier obstructions. *Phys. Rev. Lett.* **121**, 126402 (2018).
17. Bradlyn, B., Wang, Z., Cano, J. & Bernevig, B. A. Disconnected elementary band representations, fragile topology, and Wilson loops as topological indices: An example on the triangular lattice. *Phys. Rev. B* **99**, 045140 (2019).
18. Kooi, S. H., van Miert, G. & Ortix, C. Classification of crystalline insulators without symmetry indicators: atomic and fragile topological phases in twofold rotation symmetry systems. *Phys. Rev. B* **100**, 115160 (2019).
19. Bouhon, A., Black-Schaffer, A. M. & Slager, R.-J. Wilson loop approach to fragile topology of split elementary band representations and topological crystalline insulators with time-reversal symmetry. *Phys. Rev. B* **100**, 195135 (2019).
20. Ahn, J., Park, S. & Yang, B.-J. Failure of Nielsen-Ninomiya theorem and fragile topology in two-dimensional systems with space-time inversion symmetry: application to twisted bilayer graphene at magic angle. *Phys. Rev. X* **9**, 021013 (2019).
21. Song, Z.-D., Elcoro, L., Xu, Y.-F., Regnault, N. & Bernevig, B. A. Fragile phases as affine monoids: classification and material examples. *Phys. Rev. X* **10**, 031001 (2020).
22. Bouhon, A., Bzdušek, T. & Slager, R.-J. Geometric approach to fragile topology beyond symmetry indicators. *Phys. Rev. B* **102**, 115135 (2020).
23. Zhao, Y. X. & Lu, Y. *PT*-symmetric real Dirac fermions and semimetals. *Phys. Rev. Lett.* **118**, 056401 (2017).
24. Ahn, J., Kim, D., Kim, Y. & Yang, B.-J. Band topology and linking structure of nodal line semimetals with $Z_2$ monopole charges. *Phys. Rev. Lett.* **121**, 106403 (2018).
25. Wu, Q., Soluyanov, A. A. & Bzdušek, T. Non-Abelian band topology in noninteracting metals. *Science* **365**, 1273–1277 (2019).
26. Bouhon, A. et al. Non-Abelian reciprocal braiding of Weyl points and its manifestation in ZrTe. *Nat. Phys.* **16**, 1137–1143 (2020).
27. Wang, K., Dai, J.-X., Shao, L. B., Yang, S. A. & Zhao, Y. X. Boundary criticality of *PT*-invariant topology and second-order nodal-line semimetals. *Phys. Rev. Lett.* **125**, 126403 (2020).
28. Guo, Q. et al. Experimental observation of non-Abelian topological charges and edge states. *Nature* **594**, 195–200 (2021).
29. Jiang, B. et al. Experimental observation of non-Abelian topological acoustic semimetals and their phase transitions. *Nat. Phys.* **17**, 1239–1246 (2021).
30. Xie, F., Song, Z., Lian, B. & Bernevig, B. A. Topology-bounded superfluid weight in twisted bilayer graphene. *Phys. Rev. Lett.* **124**, 167002 (2020).
31. Peri, V. et al. Experimental characterization of fragile topology in an acoustic metamaterial. *Science* **367**, 797–800 (2020).
32. Ünal, F. N., Bouhon, A. & Slager, R.-J. Topological Euler class as a dynamical observable in optical lattices. *Phys. Rev. Lett.* **125**, 053601 (2020).
33. Ezawa, M. Topological Euler insulators and their electric circuit realization. *Phys. Rev. B* **103**, 205303 (2021).
34. Jotzu, G. et al. Experimental realization of the topological Haldane model with ultracold fermions. *Nature* **515**, 237 (2014).
35. Huang, L. et al. Experimental realization of two-dimensional synthetic spin-orbit coupling in ultracold Fermi gases. *Nat. Phys.* **12**, 540 (2016).
36. Meng, Z. et al. Experimental observation of a topological band gap opening in ultracold fermi gases with two-dimensional spin-orbit coupling. *Phys. Rev. Lett.* **117**, 235304 (2016).
37. Wu, Z. et al. Realization of two-dimensional spin-orbit coupling for Bose-Einstein condensates. *Science* **354**, 83 (2016).
38. Sugawa, S., Salces-Carcoba, F., Perry, A. R., Yue, Y. & Spielman, I. B. Second Chern number of a quantum-simulated non-Abelian Yang monopole. *Science* **360**, 1429 (2018).
39. Song, B. et al. Observation of symmetry-protected topological band with ultracold fermions. *Sci. Adv.* **4**, eaao4748 (2018).
40. de Léséleuc, S. et al. Observation of a symmetry-protected topological phase of interacting bosons with Rydberg atoms. *Science* **365**, 775 (2019).
41. Yuan, X.-X. et al. Observation of topological links associated with hopf insulators in a solid-state quantum simulator. *Chin. Phys. Lett.* **34**, 060302 (2017).
42. Lian, W. et al. Machine learning topological phases with a solid-state quantum simulator. *Phys. Rev. Lett.* **122**, 210503 (2019).
43. Ji, W. et al. Quantum simulation for three-dimensional chiral topological insulator. *Phys. Rev. Lett.* **125**, 020504 (2020).

44. Xin, T. et al. Quantum phases of three-dimensional chiral topological insulators on a spin quantum simulator. *Phys. Rev. Lett.* **125**, 090502 (2020).
45. Zhang, W. et al. Observation of non-hermitian topology with nonunitary dynamics of solid-state spins. *Phys. Rev. Lett.* **127**, 090501 (2021).
46. Flurin, E. et al. Observing topological invariants using quantum walks in superconducting circuits. *Phys. Rev. X* **7**, 031023 (2017).
47. Cai, W. et al. Observation of topological magnon insulator states in a superconducting circuit. *Phys. Rev. Lett.* **123**, 080501 (2019).
48. Tan, X. et al. Experimental observation of tensor monopoles with a superconducting qudit. *Phys. Rev. Lett.* **126**, 017702 (2021).
49. Niu, J. et al. Simulation of higher-order topological phases and related topological phase transitions in a superconducting qubit. *Sci. Bull.* **66**, 12 (2021).
50. Blatt, R. & Roos, C. F. Quantum simulations with trapped ions. *Nat. Phys.* **8**, 277 (2012).
51. Monroe, C. et al. Programmable quantum simulations of spin systems with trapped ions. *Rev. Mod. Phys.* **93**, 025001 (2021).
52. Alexandradinata, A., Dai, X. & Bernevig, B. A. Wilson-loop characterization of inversion-symmetric topological insulators. *Phys. Rev. B* **89**, 155114 (2014).
53. Yang, Y.-B., Li, K., Duan, L.-M. & Xu, Y. Type-II quadrupole topological insulators. *Phys. Rev. Res.* **2**, 033029 (2020).
54. Fidkowski, L. Entanglement spectrum of topological insulators and superconductors. *Phys. Rev. Lett.* **104**, 130502 (2010).
55. Turner, A. M., Zhang, Y. & Vishwanath, A. Entanglement and inversion symmetry in topological insulators. *Phys. Rev. B* **82**, 241102 (2010).
56. Wang, C., Zhang, P., Chen, X., Yu, J. & Zhai, H. Scheme to measure the topological number of a chern insulator from quench dynamics. *Phys. Rev. Lett.* **118**, 185701 (2017).
57. Moore, J. E., Ran, Y. & Wen, X.-G. Topological surface states in three-dimensional magnetic insulators. *Phys. Rev. Lett.* **101**, 186805 (2008).
58. Deng, D.-L., Wang, S.-T., Shen, C. & Duan, L.-M. Hopf insulators and their topologically protected surface states. *Phys. Rev. B* **88**, 201105 (2013).
59. Allcock, D. T. C. et al. Reduction of heating rate in a microfabricated ion trap by pulsed-laser cleaning. *N. J. Phys.* **13**, 123023 (2011).
60. Stick, D. et al. Demonstration of a microfabricated surface electrode ion trap. arXiv:1008.0990 (2010).
61. Hong, S. et al. Experimental methods for trapping ions using microfabricated surface ion traps. *J. Vis. Exp.* **126**, e56060 (2017).
62. James, D. F. & Jerke, J. Effective Hamiltonian theory and its applications in quantum information. *Can. J. Phys.* **85**, 625–632 (2007).
63. Thew, R. T., Nemoto, K., White, A. G. & Munro, W. J. Qudit quantum-state tomography. *Phys. Rev. A* **66**, 012303 (2002).

## Author contributions
L.M.D., Y. X., and Z.C.Z. supervised the project. Y.B.Y. and Y. X. performed the theoretical calculation. Y.J., Z.C.M., W.D.Z., L.H. did the fabrication of the surface trap, W.D.Z., W.X.G., L.Y.Q., G.X.W., L.Y., Z.C.Z. carried out the experiment. Y.X., W.D.Z, Y.B.Y., L.M.D. wrote the manuscript.

## Competing interests
The authors declare no competing interests.

## Additional information
**Supplementary information** The online version contains supplementary material available at https://doi.org/10.1038/s42005-022-01001-2.

**Correspondence** and requests for materials should be addressed to Zichao Zhou, Yong Xu or Luming Duan.

**Peer review information** *Communications Physics* thanks the anonymous reviewers for their contribution to the peer review of this work.

**Reprints and permission information** is available at http://www.nature.com/reprints

**Publisher's note** Springer Nature remains neutral with regard to jurisdictional claims in published maps and institutional affiliations.